



On the Computation of Turbulent Mixing Processes with Application to EGR in IC-Engines

Alexander Sakowitz

Licentiate Thesis

November 2011
Technical reports from
Royal Institute of Technology
Department of Mechanics

Postal address	Visiting address	Contact
Royal Institute of Technology Mekanik SE-100 44 Stockholm Sweden	Osquarsbacke 18 Stockholm	+46 8 790 6188 sakowitz@mech.kth.se

Akademisk avhandling som med tillstånd av Kungliga Tekniska Högskolan i Stockholm framlägges till offentlig granskning för avläggande av teknologie licentiatexamen fredag den 2 december 2011 kl 10.15 i sal E51, Osquarsbacke 14, Kungliga Tekniska Högskolan, Stockholm.

TRITA-MEK Technical report 2011:14

ISSN 0348-467X

ISRN KTH/MEK/TR-11/14-SE

ISBN 978-91-7501-180-6

©Alexander Sakowitz 2011

Universitetsservice US-AB, Stockholm 2011

On the Computation of Turbulent Mixing Processes with Application to EGR in IC-Engines

Alexander Sakowitz 2011

KTH Department of Mechanics
SE-100 44 Stockholm, Sweden

Abstract

This thesis deals with turbulent mixing processes occurring in internal combustion engines, when applying exhaust gas recirculation (EGR). EGR is a very efficient way to reduce emissions of nitrogen oxides (NO_x) in internal combustion engines. Exhaust gases are recirculated and mixed with the intake air of the engine, thus reducing the oxygen concentration of the combustion gas and the maximum combustion temperature. This temperature decrease results in a reduction of NO_x emissions, since NO_x is produced at high temperatures.

The issue of NO_x reduction is of high importance for current engine development (particularly for heavy-duty engines), since NO_x is the main cause for smog formation and subject to increasingly stronger emission legislation. One of the practical problems when applying EGR is the non-uniformity of the mixture among and inside the cylinders deteriorating the engine and emission performance.

The aim of this work is to develop and assess methods suited for the computation of turbulent mixing processes in engine conditions. More specifically, RANS and LES computations are considered. The flow structures responsible for the mixing are analyzed for two different T-junctions and a six-cylinder Scania engine-manifold. Shortcomings and advantages of the applied mixing models are explained.

The main results are, that commonly applied scalar flux models for the RANS framework do not predict correct scalar flux directions. In stationary flow, the applied k - ϵ -model in combination with a gradient-diffusion-model gives too small mixing rates as compared to LES and experiments. Furthermore, the LES computations of the T-junctions show, that Dean vortices occurring due to the curvature of the flow are broken up and dissipated only a few diameters downstream of the junction. The RANS computations do not predict this break-up, giving fundamentally different flow structures and mixing distributions. In pulsating flow, a resonance between the natural stabilities and the pulsation frequency is found by LES results, which could not be predicted by RANS.

Computations of the flow in a Scania intake manifold with generic boundary conditions indicate, that inlet pulsations are important for the mixing process and that the smoothing effect of URANS is not adequate for accurate mixing computations. LES, on the other hand, is more promising, since it is able to capture the physics of pulsating flows much better.

Descriptors: Turbulent mixing, Large eddy simulation, IC-engines, T-junction

Preface

This licentiate thesis consists of two parts. The first part gives an introduction into the field of emission formation in internal combustion engines and the computation of mixing processes. The second part consists of two papers, discussing LES and RANS computations in more detail. The work presented in this thesis has been performed by the author under supervision of Laszlo Fuchs. The simulations work was done using the OpenFOAM ®environment.

November 2011, Stockholm
Alexander Sakowitz

Contents

Abstract	iii
Preface	iv
Part 1. Overview and Summary	1
Chapter 1. Introduction	2
Chapter 2. Emissions of Internal Combustion engines	4
2.1. IC engine cycles	4
2.2. Combustion and emissions	5
2.3. Reduction of emissions	7
Chapter 3. Turbulence and turbulent mixing	11
3.1. The energy cascade and Kolmogorov's hypotheses	11
3.2. Turbulent mixing	13
Chapter 4. Computation of turbulent mixing	15
4.1. Governing equations	15
4.2. Modeling of turbulence and turbulent mixing	16
4.3. Boundary conditions	20
4.4. Numerics	21
4.5. Evaluation of mixing quality	24
Chapter 5. Computations and Results	26
5.1. Mixing process in a T-junction with square cross-section	26
5.2. Mixing process in a T-junction with circular cross-sections	29
5.3. Comparison of the mixing quality for the two junctions (stationary flow)	37
5.4. Scania Manifold	39
Chapter 6. Conclusions and outlook	41

Acknowledgements	43
References	44
Part 2. Papers	47
Paper 1 - LES of the turbulent mixing process in a T-junction with stationary and pulsating inflow conditions	49
Paper 2 - Computation of mixing processes related to EGR	68

Part 1

Overview and Summary

CHAPTER 1

Introduction

Mixing processes are of high importance in numerous technical applications. Some examples are the mixing of air and fuel in gas turbines or internal combustion engines, mixing of hot and cold water in power plant applications, or chemical applications, where the mixing quality of two reacting substances determines the reaction rate. This thesis deals with the mixing process occurring in Exhaust Gas Recirculation (EGR) applications. EGR is a relatively new means of reducing NO_x emissions of internal combustion engines (ICE). The working principle is illustrated in fig. 1.1. A portion of the exhaust gases is recirculated and mixed with the intake air. Inhomogeneity of this mixture has a deteriorating effect on the engine performance and the engine emissions, shown experimentally by Maiboom *et al.* (2009).

NO_x emissions are the main cause for smog emissions and are problematic for both Diesel and Otto engines. Car and truck manufacturers are therefore facing strong regulations on the limits of NO_x emissions. Thus, the understanding, prediction and optimization of the mixing process between EGR and air is of high interest for industrial applications. Other issues with EGR, not addressed in this thesis, are the condensation of water contained in the exhaust gases and the deposition of soot particles.

The aim of this thesis is to examine mixing processes in engine-like conditions and to assess different modeling approaches, namely RANS and LES. Furthermore the physics governing the mixing are analyzed based on these computations. Apart from the modeling approach, the boundary conditions are crucial when performing numerical simulations because the real boundary conditions as they occur in an engine are difficult to determine and have to be estimated.

The approach is to compute mixing processes in simplified geometries, first in stationary flow, thereafter in pulsating flow in order to study the mechanisms governing the mixing quality. In all cases, the EGR concentration is treated as a passive scalar. The different modeling approaches are compared to experimental data when available. Finally, LES and RANS computations are performed for an inlet manifold of a 6-cylinder Scania engine and the mixing quality is evaluated for different boundary conditions.

Mixing of passive scalars in junctions under stationary flow conditions have been investigated in numerous computational and experimental studies. A good overview

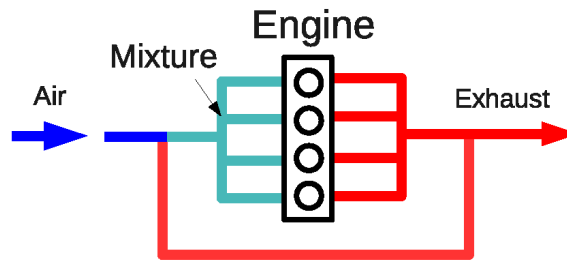


FIGURE 1.1. Exhaust gas recirculation

of the available literature is given in Hu & Kazimi (2006). Recently, mixing predictions with RANS models have been investigated by Walker *et al.* (2010), showing that the RANS models need ad-hoc adjustment of the model constants in order to match experimental results.

LES has been applied among others by Hu & Kazimi (2006), Kuczaj *et al.* (2010) and Westin *et al.* (2008). LES was shown to be a promising approach for the predictions of turbulent mixing.

The literature available about mixing scalars under pulsating flow conditions and engine-like conditions is scarce. Yoshizawa *et al.* (2003) performed URANS computations for EGR distribution predictions in ICE and studied the influence of geometrical parameters. Similar work was performed quite recently by Karthikeyan *et al.* (2011), predicting significant inhomogeneity regarding the EGR distribution among the cylinders. However, no study of the accuracy of the numerical method and the applied turbulence models was found, which is the main contribution of this work.

The thesis will start with an introduction to emission formation and the most common ways of emission reduction. Thereafter, some theoretical aspects of turbulence and passive scalar mixing are treated. Chapter 4 will introduce the concepts used for the computation of turbulent flows and mixing processes. The results are summarized in chapter 5 and finally chapter 6 will conclude the thesis by summarizing the most important conclusions and giving a perspective on future work.

CHAPTER 2

Emissions of Internal Combustion engines

This chapter covers the basics regarding emission formation in internal combustion engines (ICE). First, the working principle of ICE is introduced and the description of engine cycles is treated. Thereafter, the problematic emissions and the most common approaches to their reduction are discussed shortly. A more detailed description is given in e.g. Reifarth (2010).

2.1. IC engine cycles

Internal combustion engines convert chemical energy bound in fuel into mechanical energy. This is achieved by combustion of fuel delivering heat to the combustion gas. The increase of thermal energy of the gas results in a drastic pressure increase used to perform work on a piston through gas expansion. In this way the combustion gas works as the operating medium. In order to produce work continuously this process has to be cyclic, i.e. the working medium has to return to its initial condition. The return to the initial condition in an ICE is obtained by an exchange of the working medium after each cycle (open cycle). The four-stroke engine is the most common ICE consisting of an intake stroke, a compression stroke, an expansion stroke and an exhaust stroke. One cycle consists therefore of two revolutions; one for generation of work and one for the gas exchange process.

Ideally, the engine cycle can be split up into four parts. Isentropic compression (1-2), combustion (2-3), isentropic expansion (3-4) and isochoric reversion (4-1). The combustion process can be assumed to be either isochoric or isobaric. Isochoric combustion corresponds to an infinitely fast combustion whereas isobaric combustion represents a very slow combustion process. The real combustion process is somewhere in between these processes.

From the isochoric assumption, one gets the ideal cycle for the constant-volume process, i.e. combustion takes place at a constant volume, which would be equivalent to an infinitely rapid heat supply. Further assumptions in this description are constant specific heats c_p and c_v and negligible heat and flow losses. The constant-volume-cycle is shown in the p-V-diagram (see fig. 2.1), together with the constant-pressure-cycle shown in fig. 2.2.

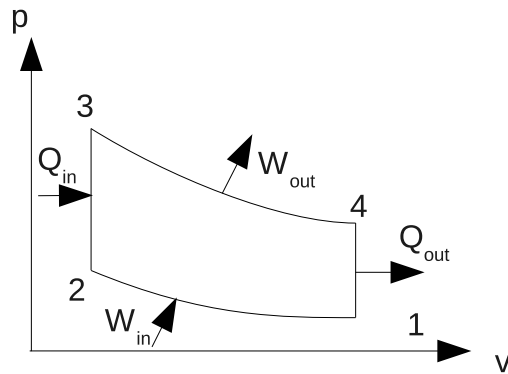


FIGURE 2.1. The ideal constant-volume cycle

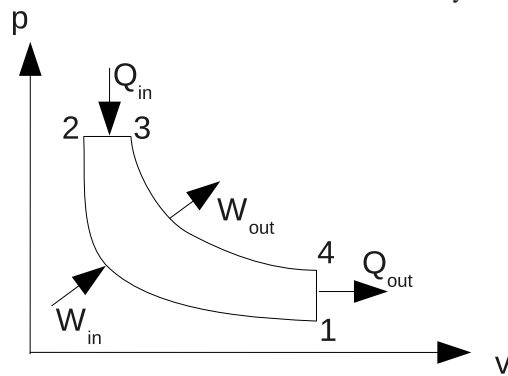


FIGURE 2.2. The ideal constant-pressure cycle

A real engine cycle will of course differ from the assumptions above and will rather resemble the cycle depicted in fig. 2.3. This cycle is subject to fluid, thermodynamic and mechanical losses and comprises also the gas exchange cycle (see Dietsch & Klingebiel (2007) and Heywood (1988)).

2.2. Combustion and emissions

Combustion is the chemical reaction that occurs between a fuel and an oxidizing agent that releases energy, usually in the form of heat and light. There are two generally different types of combustion in ICE, spark-ignited (SI) and compression-ignited (CI) combustion. The first one is usually associated with Otto- or gasoline engine, the latter with Diesel engines. In SI-combustion the flame starts at the spark and travels through the combustion chamber. Usually, the fuel is premixed with air in the intake manifold. In CI engines the fuel is injected directly into the combustion chamber, when high pressures and temperatures are already reached. The mixture of fuel and

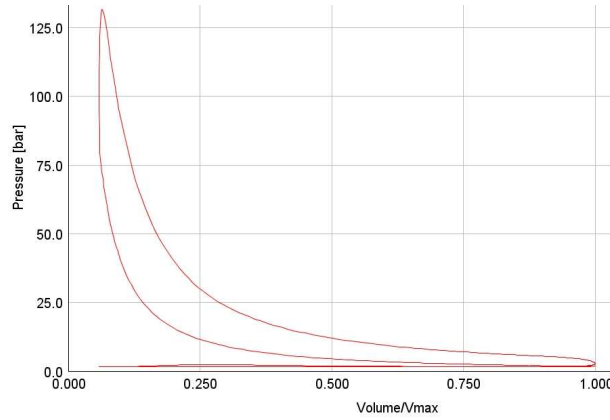


FIGURE 2.3. p-v-diagram for real engine (Courtesy of Simon Reifarth)

hot gases is then ignited by itself. Diesel engines can reach much higher efficiencies than gasoline engines, because higher pressure ratios can be reached. In gasoline engines the pressure ratio is limited by unwanted self-ignition of the fuel.

An important parameter for the combustion and the emission formation is the air/fuel ratio λ defined as

$$\lambda = \frac{m_{air}}{m_{fuel} \cdot Z}, \quad (2.1)$$

where m_{air} and m_{fuel} represent the mass of air and fuel participating in the combustion and Z is the stoichiometric factor. If $\lambda = 1$, the amount of fuel corresponds exactly to the amount of air needed for complete combustion, i.e. all oxygen and fuel present in the combustion chamber are burned. If $\lambda > 1$, there is an excess of air, whereas $\lambda < 1$ represents an incomplete combustion due to too small amounts of air. Gasoline engines are usually operated at $\lambda = 1$, whereas Diesel engines usually have a higher $\lambda (> 1.2)$ in order to ensure complete combustion with fuel injection. For premixed combustion, λ is approximately constant over the combustion chamber whereas in a heterogeneous mixture λ may range locally from 0 to infinity, which is the case for direct fuel injection.

For SI-engines, the formation of emissions is highly dependent on λ . CI engines have very different emission characteristics as compared to SI engines. The emission formation in CI combustion is more dependent on the local λ .

Complete combustion at $\lambda = 1$ would produce only carbon dioxide (CO_2) and water. However, complete combustion is difficult to achieve and real combustion is always accompanied by unwanted emissions. Pollutant emissions regulated by legislation inside the EU, USA and Japan are: Particulate matter (PM), Nitric Oxides (NO_x), Hydrocarbons (HC) and Carbon monoxide (CO).

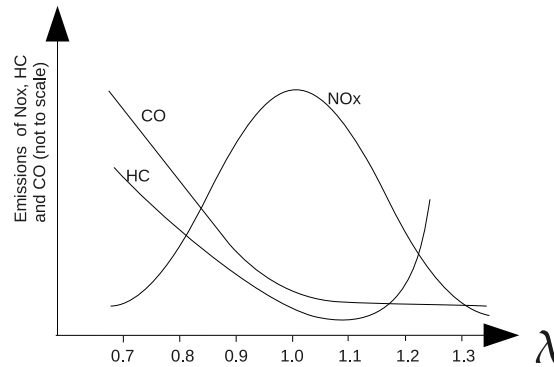


FIGURE 2.4. Dependency of emissions on λ for SI-engines

For Diesel combustion, the most problematic emissions are PM and NO_x . SI engines are primarily producing NO_x , CO, and HC emissions, whereas PM is not a big problem for SI engines.

NO_x is a common designation for the nitrogen oxides NO and NO_2 . NO_x emissions occur at high combustion temperatures. Nitrogen (N_2) reacts with oxygen at temperatures higher than 2200 K. High combustion temperatures occur when λ is around 1, i.e. the reaction rate is high, since there are a lot of oxygen molecules available for the fuel to react with. For higher λ , the maximum combustion temperature and so the NO_x emissions are decreasing again due to higher fuel dilution. The decrease of NO_x emissions is a challenge for both Diesel and SI engines, since NO_x emissions are the primary reason for smog.

CO occurs at low λ , due to incomplete oxidation. Thus, CO emissions are not problematic in Diesel engines. If CO is inhaled it binds with the red blood cells instead of oxygen, which can be lethal for high doses.

HC is a product of incomplete combustion at both high and low λ . HC is highly carcinogenic and is causing smog. HC is more problematic for SI engines.

Fig. 2.4 summarizes the λ -dependency of the different emissions for SI engines. CI engine emissions differ quantitatively from SI engines and are less dependent on λ . For example, NO_x emissions are about one order of magnitude greater in CI engines (see e.g. Heywood (1988)).

2.3. Reduction of emissions

Since emissions of pollutants are hazardous for the environment and humans, engine manufacturers had and will have to cope with drastic decreases of the legal emission limits. Fig. 2.5 shows the development of the allowed PM and NO_x emissions from 1996 to 2014.

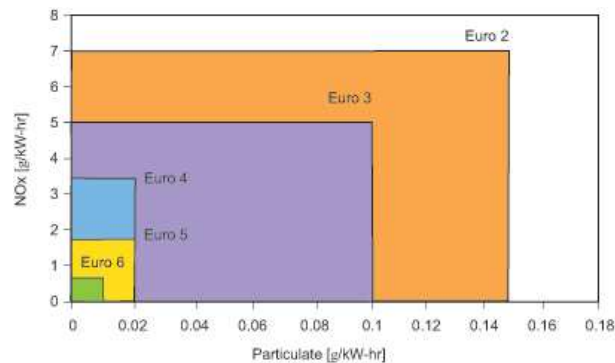


FIGURE 2.5. Emission reduction from 1996 (Euro 2) until 2014 (Euro6)

Some of the most common and promising approaches to the problem are summarized in this section. EGR, which is the main focus of this thesis, is described more in detail.

2.3.1. *New combustion modes*

Perhaps the most obvious way to reduce emissions is to obtain a cleaner and more complete combustion. A still fairly undeveloped approach is Homogenous Charge Compression Ignition (HCCI). It combines the principles of SI and Diesel engines as it uses a premixed fuel/air mixture and autoignition. This can be achieved by injecting the fuel very early during the compression stroke. Advantages with this approach are dramatically improved NO_x and PM emissions due to a more homogenous combustion avoiding high peak temperatures. However, the combustion phasing is difficult to control, since it is determined solely by the fuel mixture and the compression ratio (see Stanglmaier & Roberts (1999)).

An even more complex proposal in order to control the autoignition event is Partially Premixed Compression Ignition (PPCI). The idea is to control the injection event such that the combustible mixture is not completely homogeneous at the time of ignition, rather only 'partially' premixed. This leads to occurrence of richer and leaner regions within the combustion chamber, causing the combustion to start at several regions simultaneously, thus slowing down the combustion and the heat release (see Stanglmaier & Roberts (1999)).

The approach of stratified combustion is to use and control fuel injection in SI-engines in such way that there are different layers within the combustion chamber with richer mixture close to the spark and leaner mixture as the flame is spreading. High combustion temperatures can thereby be avoided. These techniques are very difficult to control and are still in the development phase.

2.3.2. After-treatment

After-treatment of exhaust gases denotes the reduction of emissions contained in the exhaust gases after combustion. This can be achieved by catalyzers, filters and/or reducing agents. An oxidation catalyst is able to significantly lower emissions of CO and HC. A three-way catalyst further improves the reduction of NO_x emissions. However, a prerequisite for efficient operation of the three-way-catalyzer is that $\lambda \sim 1$. Its use is therefore limited to SI engines. An additional way to significantly lower NO_x emissions is Selective Catalytic Reduction (SCR). A reducing agent, most often ammonia (NH₃) formed from urea, is injected into the exhaust gases and selectively oxidizes with the oxygen contained in the nitrogen oxides (see Dietsch & Klingebiel (2007)). The disadvantage with SCR is that urea has to be transported in the vehicle and refilled. Furthermore, there are issues due to crystallization of urea in cold start, that can cause blockage of the exhaust piping.

2.3.3. Exhaust Gas Recirculation

One of the easiest and most efficient ways to reduce NO_x emissions is to lower the oxygen concentration during combustion by EGR. Exhaust gases are recirculated and mixed with the intake air prior to combustion. The introduction of inert exhaust gas slows down the reaction rate during combustion since there are less oxygen molecules available for the reaction. Moreover, the heat capacity (c_p) of the mixture is increased due to the presence of exhausts in the mixture. These effects lead to a reduction of the peak temperatures during the combustion, thus decreasing the NO_x emissions.

EGR is mainly used in CI engines. However, EGR is also promising in SI engines for NO_x reduction in regimes where catalyzers do not work and for decreasing throttle losses (if EGR is present the throttle has to be opened further). Recently, Chauvet & Dimitrova (2008) showed that the addition of cooled EGR in SI-engines at high loads can result in a decrease of fuel consumption up to 20% since excessive over-fueling needed for the reduction of the exhaust temperatures is avoided¹.

EGR can be achieved internally by valve overlap or externally through a connection between the exhaust pipe and the intake manifold, where an EGR valve controls the EGR flow. In combination with a turbocharger, it is possible to introduce the exhaust gases upstream or downstream of the turbocharger. The first is referred to as long-route EGR, the latter as short-route EGR. Even though long-route EGR offers some advantages in terms of engine efficiency, short-route is still the state-of-the-art, mainly because the introduction of exhausts and soot into the compressor is not desirable.

Limits on the amount of EGR are given by misfire due to lack of oxygen, resulting in higher HC emissions (see Schwarz *et al.* (1988)). Furthermore, high EGR rates will decrease the engine efficiency through pump losses.

¹For SI engines at high loads, it is common to inject more fuel than actually needed in order to avoid high exhaust temperatures that can damage the catalyzer

Another issue regarding the use of EGR is the mixing quality between exhaust gas and air. This is the topic of this thesis. Non-uniform mixtures of air and exhaust gases are problematic, since they will influence the engine performance and emissions. The mixture can be non-uniformly distributed among the cylinders as well as inside the combustion chamber that can lead to misfire and increased NO_x emissions.

Turbulence and turbulent mixing

Turbulence characterizes the chaotic and unsteady motion found in most technical fluid flow applications. Turbulence occurs when the inertial forces are much greater as compared to the viscous ones. Thus, the most important parameter of turbulence is the Reynolds number giving the ratio of the inertial forces to the viscous forces,

$$Re = \frac{\mathcal{U} \cdot \mathcal{L}}{\nu}, \quad (3.1)$$

where \mathcal{U} is a characteristic velocity and \mathcal{L} a characteristic length of the flow. \mathcal{L} corresponds to the largest scales of the flow. If the Reynolds number is high enough, the flow is turbulent, i.e. even in simple flow situations, as pipe flow, the velocity field can be highly unsteady and chaotic.

Characteristic for turbulence is the presence of fluid motion within a large range of scales. An increase of the Reynolds number will increase the range of scales of the turbulent motions, i.e. with increasing Reynolds number, the smallest scales, at which dissipation occurs, are decreasing.

This chapter introduces Kolmogorov's hypotheses, used to estimate the smallest scales of the turbulent motions and the energy transport from larger to smaller scales. Corresponding considerations are introduced for the passive scalar mixing, based on Batchelor's ideas.

3.1. The energy cascade and Kolmogorov's hypotheses

Important facts concerning turbulence are the existence of a broad range of scales in the fluid motion and the transport of energy from larger to smaller scales, i.e. large eddies break up into smaller eddies. However, the bulk of the kinetic energy is contained in the largest scales, governed by the boundary conditions. At sufficiently high Reynolds numbers, the statistics of the smallest scales can be assumed to be isotropic and independent of the boundary conditions, i.e. all information about direction is lost in the break-up process. From these arguments it can be concluded that the small scales are universal, i.e. the small scales have a similar behavior in all flow realizations.

The energy transfer starts at the largest scales and continues until viscous dissipation takes over. Since viscous effects occur only at the smallest scales, an estimation of the smallest scales can be made from dimensional analysis following Kolmogorov's first hypothesis. Kolmogorov's first hypothesis states that at sufficiently high Reynolds number, the smallest scales are only dependent on the dissipation rate ϵ and the

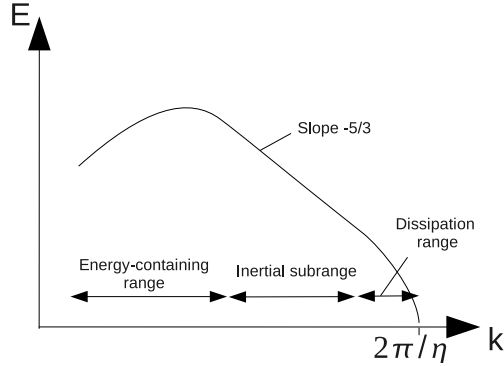


FIGURE 3.1. The turbulent energy spectrum

kinematic viscosity ν (see Kolmogorov (1991)¹). From dimensional arguments, it can be found that the only possible way to form length, velocity and time scales from ϵ and ν are

$$\eta = \left(\frac{\nu^3}{\epsilon}\right)^{\frac{1}{4}} \quad (3.2)$$

$$u_\eta = (\epsilon\nu)^{\frac{1}{4}} \quad (3.3)$$

$$\tau_\eta = \left(\frac{\nu}{\epsilon}\right)^{\frac{1}{2}}. \quad (3.4)$$

When in equilibrium, the energy transfer between the scales must equal the dissipation rate. At intermediate scales ($\mathcal{L} \gg l_o \gg \eta$), too small for the boundary conditions to affect their behavior, and too large for viscous effects to take place, the energy transfer can only depend on the dissipation rate ϵ . This is Kolmogorov's second hypothesis (see Kolmogorov (1991)). This range is called the inertial subrange.

Statistics of turbulence are often analyzed in the frequency domain. The energy spectrum $E(k)$ gives the distribution of turbulent kinetic energy over the range of frequencies or wave numbers k of the turbulent scales. The length scale and the wave number are related through $k = 2\pi/l$.

From Kolmogorov's second hypothesis and dimensional analysis the following relation is found:

$$E(k) \propto \epsilon^{2/3} k^{-5/3}, \quad (3.5)$$

which gives the slope of the energy spectrum.

A qualitative sketch of the energy spectrum is shown in fig. 3.1. The inertial subrange has a slope of $k^{-5/3}$ up to the smallest scales given by $2\pi/\eta$. For a more detailed description of turbulence the reader is referred to e.g. Pope (2008).

¹Translation of russian original from 1941

3.2. Turbulent mixing

Turbulent mixing designates the mass transport due to turbulence. In general, reactive mixing can be distinguished from passive mixing. In reactive mixing the mass transport influences the flow properties, whereas in passive mixing, as the name indicates, the transport is passive, i.e. it does not influence the flow field. This thesis will only consider passive mixing. The mechanisms governing the passive mixing are advection and molecular diffusion. Advection is the transport of mass by the flow and particularly by turbulence. Molecular diffusion is the process caused by motions on the molecular level (Brownian motion). In fluids, molecules are constantly moving in all directions and interacting with other molecules. In the presence of two species this motion gives a net transport from one species to the other one. In the absence of high temperature and pressure gradients, molecular diffusion acts against the gradient of the transport quantity and the resulting flux is proportional to the gradient of the transport quantity (concentration). Thus, the flux J_i can be expressed by Fick's law,

$$J_i = -\kappa \frac{\partial \phi}{\partial x_i}, \quad (3.6)$$

where κ is the diffusion coefficient and ϕ is some transported scalar (e.g. a concentration)².

For high Reynolds numbers, molecular diffusion is much slower than advection. Thus, molecular diffusion can only act on the smallest scales. An important dimensionless number is the Schmidt number,

$$Sc = \frac{\nu}{\kappa}, \quad (3.7)$$

representing the ratio between momentum diffusivity and molecular diffusivity. Typical values for Sc are approximately unity for gases and in the order of 1000 for liquids. The value of the Schmidt number is temperature and pressure dependent. However, this is neglected throughout this thesis.

In the case of $Sc < 1$, the smallest scales of the transport scalar are diffused faster than those of the velocities. The energy spectrum of the scalar fluctuations must therefore have a lower cut-off wave number as compared to the velocity spectrum. $Sc > 1$ displays the opposite behavior and much smaller scales are present in the scalar spectrum (greater wave lengths). The slope of the energy spectrum is -1 for wave lengths beyond the Kolmogorov scales, which can be shown from dimensional arguments. For smaller wave lengths, where diffusion is negligible, the scalar spectrum shows the same behavior as the velocity spectrum. Fig. 3.2 shows the theoretical scalar spectrum for the different Schmidt number regimes.

This behavior was first predicted by Batchelor (1959) and Batchelor *et al.* (1959), who also derived the smallest scales of the scalar spectrum, which differ from the Kolmogorov scales for $Sc \neq 1$. The Batchelor scales can be expressed in terms of the

²This is equivalent to heat conduction, which is the reason why the temperature in incompressible flows can be treated as a passive scalar

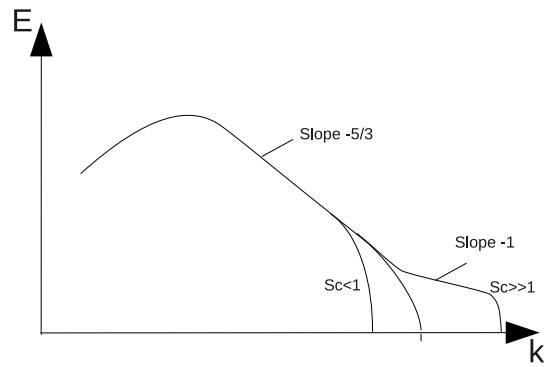


FIGURE 3.2. The scalar energy spectrum

Kolmogorov scales and the Schmidt number as

$$\lambda_B = \left(\frac{\nu \kappa^2}{\epsilon} \right)^{1/4} = \eta \cdot Sc^{-1/2}, \text{ for } Sc \gtrsim 1 \quad (3.8)$$

and

$$\lambda_B = \left(\frac{\kappa^3}{\epsilon} \right)^{1/4} = \eta \cdot Sc^{-3/4}, \text{ for } Sc < 1. \quad (3.9)$$

Computation of turbulent mixing

In order to compute turbulent mixing process, the equations governing the flow (and the turbulence) have to be solved. Additionally to the flow equations, an equation for the mixing scalar is solved. Several approaches to the numerical solution of these equations have been proposed. The approaches can be categorized into three groups; Direct numerical simulation (DNS), Large eddy simulations (LES) and Reynolds averaged Navier-Stokes (RANS) computations.

In DNS all scales are resolved, thus no modeling is needed. This is, however, very computational expensive since the smallest scales decrease with increasing Reynolds number (see chapter 3). It can be shown that the computational costs scale with the Reynolds number as Re^3 making DNS unfeasible for high Reynolds numbers.

LES is an approach in order to circumvent the difficulties in DNS by resolving only the scales that carry the major part of the turbulent kinetic energy. The effect of the unresolved scales on the resolved scales is modeled by a sub-grid-scale (SGS) model. In a RANS, the equations for the ensemble-averaged equations are solved, i.e. all scales of turbulent motion are modeled.

This chapter introduces the governing flow equations. Thereafter, the LES and RANS models handling turbulence and turbulent mixing are described. Finally, the boundary conditions and the numerical methodology are discussed.

4.1. Governing equations

The Navier-Stokes-equations for a Newtonian and compressible flow, based on conservation of mass, momentum and energy are

$$\frac{\partial \rho}{\partial t} + \frac{\partial}{\partial x_j} [\rho u_j] = 0 \quad (4.1)$$

$$\frac{\partial}{\partial t} (\rho u_i) + \frac{\partial}{\partial x_j} [\rho u_i u_j + p \delta_{ij} - \tau_{ji}] = 0, \quad i = 1, 2, 3 \quad (4.2)$$

$$\frac{\partial}{\partial t} (\rho e_0) + \frac{\partial}{\partial x_j} [\rho u_j e_0 + u_j p + q_j - u_i \tau_{ij}] = 0, \quad (4.3)$$

where ρ is the density, u_i is the velocity component in i -direction, e_o is the total energy defined as $e_o = e + \frac{1}{2}u^2$, e is the internal specific energy, p is the static pressure, τ_{ij} is the viscous stress tensor and q_i is the heat flux. In a newtonian fluid the viscous

stresses are proportional to the strain rate. With the definition of the strain rate tensor

$$S_{ij} = \frac{1}{2} \left(\frac{\partial u_i}{\partial x_j} + \frac{\partial u_j}{\partial x_i} \right), \quad (4.4)$$

τ_{ij} can be written as

$$\tau_{ij} = 2\mu(S_{ij} - \frac{1}{3}S_{kk}\delta_{ij}). \quad (4.5)$$

Moreover, for the compressible form of the Navier-Stokes-equations, an equation of state is necessary in order to close the equations. In normal temperature ranges, the ideal gas equation gives sufficient accuracy:

$$p = \rho RT, \quad (4.6)$$

where R is the specific gas constant and T is the temperature.

As mentioned in the previous chapter, the passive scalar is governed by the advection-diffusion-equation. In general, the scalar equation is written as

$$\frac{\partial \rho \phi}{\partial t} + \frac{\partial \rho u_i \phi}{\partial x_i} = \frac{\partial}{\partial x_i} \rho \kappa \frac{\partial \phi}{\partial x_i}. \quad (4.7)$$

Assuming a constant Schmidt number, defined as

$$Sc = \frac{\mu}{\rho \kappa}, \quad (4.8)$$

and a constant viscosity $\mu = const.$, equation 4.7 can be rewritten as

$$\frac{\partial \rho \phi}{\partial t} + \frac{\partial \rho u_i \phi}{\partial x_i} = \frac{\mu}{Sc} \frac{\partial^2 \phi}{\partial x_i^2}. \quad (4.9)$$

By using partial derivation and the continuity equation this simplifies to:

$$\frac{\partial \phi}{\partial t} + u_i \frac{\partial \phi}{\partial x_i} = \frac{\nu}{Sc} \frac{\partial^2 \phi}{\partial x_i^2}, \quad (4.10)$$

with $\nu = \mu/\rho$.

Normalizing the variables u_i , x_i and t by the velocity, length and time scales

$$u_i^+ = \frac{u_i}{\mathcal{U}}, \quad x_i^+ = \frac{x_i}{\mathcal{L}}, \quad t^+ = t \frac{\mathcal{U}}{\mathcal{L}} \quad (4.11)$$

and inserting into eq. 4.9 yields the scalar equation in its non-dimensional form:

$$\frac{\partial \phi}{\partial t^+} + u_i^+ \frac{\partial \phi}{\partial x_i^+} = \frac{1}{Re \cdot Sc} \frac{\partial^2 \phi}{\partial x_i^+ \partial x_i^+} \quad (4.12)$$

The product of the Reynolds number and the Schmidt number occurring in eq. 4.11 is also denoted Peclet number $Pe = Re \cdot Sc$. From eq. 4.11 it is obvious that the diffusion term is small when the Peclet number is large.

4.2. Modeling of turbulence and turbulent mixing

As mentioned earlier in this chapter, direct numerical simulations of turbulent flows at high Reynolds numbers are not feasible due to the high demands on computational resources¹. Thus, it is necessary to introduce models in order to facilitate less computational demanding simulations.

4.2.1. RANS

Ensemble-averaging of the Navier-Stokes equation yields the so called Reynolds equations. The Reynolds equations differ from the Navier-Stokes equations through the occurrence of an additional unclosed term, the so called Reynolds stresses given by $\overline{u'_i u'_j}$, where the overbar denotes the averaging of the quantity below. For more details see e.g. Pope (2008). The Reynolds stress term has to be modeled. During the past five decades, many turbulence models have been suggested throughout literature. However, none of the proposed models are universally applicable to all flow problems (see e.g. Schäfer (1999)).

A commonly used RANS model is the k- ϵ -model, which will be presented here. The k- ϵ -model is based on the turbulent-viscosity hypothesis (Boussinesq's hypothesis), assuming an analogy between the Reynolds-stresses and the viscous stresses in an Newtonian fluid (see equation 4.5):

$$\overline{u'_i u'_j} - \frac{2}{3} k \delta_{ij} = -2\nu_t \overline{S_{ij}}, \quad (4.13)$$

where ν_t is called the turbulent viscosity. However, there is an important difference when compared with the molecular viscosity; ν_t is not a fluid property, it is a property of turbulence. Thus, it is a function of position (and time). The specification of ν_t is the subject of all turbulent-viscosity-models. In the case of the k- ϵ -model, equations for k and ϵ are formulated on the basis of empirical relations. The turbulent viscosity is specified as

$$\nu_t = C_\mu k^2 / \epsilon, \quad (4.14)$$

with $C_\mu = 0.09$.

The k- ϵ -model needs five model constants that are all calibrated against simple flow cases. The model can therefore not be expected to be valid in complex geometries with high degrees of anisotropy.

Similar to the Reynolds stresses, an additional term occurs when applying ensemble-averaging to the passive scalar equation, 4.9. The resulting equation is:

$$\frac{\partial \overline{\phi}}{\partial t} + \overline{u_i} \frac{\partial \overline{\phi}}{\partial x_i} = \frac{\nu}{Sc} \frac{\partial^2 \overline{\phi}}{\partial x_i^2} + \frac{\partial \overline{u'_i \phi'}}{\partial x_i} \quad (4.15)$$

The last term in eq. 4.14 is the turbulent flux vector, a term that is unknown and therefore has to be modeled. The most basic approach is the so-called gradient diffusion

¹For high Schmidt numbers this problem is even more severe due to the Batchelor scale (see eq. 3.8) being even smaller as compared to the Kolmogorov scale.

model (GDM). This model relies on the assumption that the turbulent flux vector is aligned with the scalar gradient, analogous to molecular diffusion:

$$\overline{u'_i \phi'} = -\kappa_t \frac{\partial \bar{\phi}}{\partial x_i}, \quad (4.16)$$

where κ_t is computed from the turbulence characteristics delivered by the turbulence model. For the $k - \epsilon$ model it is

$$\kappa_t = \frac{\nu_t}{Sc_t} = \frac{C_\mu}{Sc_t} \frac{k^2}{\epsilon}, \quad (4.17)$$

containing the turbulent Schmidt number Sc_t , a model constant. Commonly, an empirical value of $Sc_t = 0.9$ is used. However, it should be noted that the assumption of gradient-diffusion is only valid for isotropic turbulence. Even in simple shear flows, deviation from this assumption can be observed (see Pope (2008)).

An advancement of the GDM is the generalized gradient diffusion model (GGDM). It includes the effects of anisotropy by involving the Reynolds stresses

$$\overline{u'_i \phi'} = -C_h \overline{u'_i u'_j} \frac{k}{\epsilon} \frac{\partial \bar{\phi}}{\partial x_i}, \quad (4.18)$$

where C_h is a model constant, usually 0.3. The product of the Reynolds stress tensor and the scalar gradient in eq. 4.17 provides a flux vector that is not aligned with the scalar gradient if there is significant anisotropy present in the flow.

Common for all RANS-models are the numerous assumptions and empiricism needed in order to close the equations. Some of these assumptions, as the gradient diffusion assumption, are not justified by physics. Their only justification is the lack of a better assumption and/or simplicity. The big advantage with the RANS approach is that all turbulent fluctuations are filtered out and therefore do not have to be resolved. This in turn leads to low computational costs.

4.2.2. LES

DNS is computationally expensive for high Reynolds numbers and RANS is lacking generality due to the numerous models and assumptions needed. Large Eddy simulation (LES) was developed in order to overcome the shortcomings of RANS and avoiding being as computationally expensive as DNS. In LES, the large energy containing scales (or eddies) are resolved, whereas the effect of the unresolved scales on the resolved scales is modeled. This is possible because the small scales have a universal and isotropic character (see chapter 3). Hence, the small scales are rather independent of the boundary conditions.

The principle of LES is shown in fig. 4.1. The large scales are directly resolved, whereas the scales smaller than a filter width $\hat{\Delta}$ are removed by some filtering operation. This spatial filtering operation can be performed explicitly or implicitly. The filtering of the Navier-Stokes-equations leads to residual stresses τ^r on the right hand

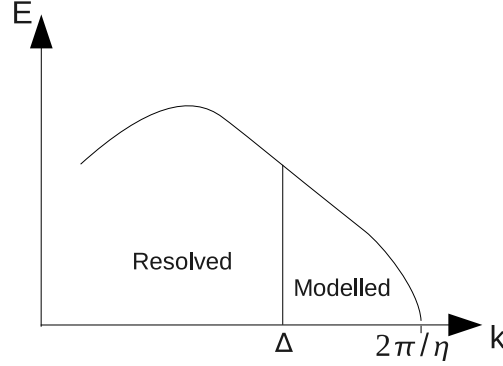


FIGURE 4.1. The turbulent energy spectrum for LES

side of the momentum equation, similar to the Reynolds stresses for RANS. The residual stresses have to be modeled in a way, that reflects the impact of the small scales on the resolved scales. Models for τ^r have to fulfill the following characteristics:

- They have to mimic the dissipation, that occurs at the small scales. I.e. they have to drain energy from the large scales.
- At the limit $\tilde{\Delta} \rightarrow 0$, the residual stresses should vanish since approaching DNS.
- Ideally, backscatter should be allowed, i.e. intermittent transport of energy from the unresolved to the resolved scales.

One of the simplest and first models proposed is the Smagorinsky model, a model introducing an eddy-viscosity ν_r analogous to the turbulent viscosity in RANS. The residual stresses are then written:

$$\tau_{ij}^r = -2\nu_r \tilde{S}_{ij} \quad (4.19)$$

where the tilde designates the filtering operation. ν_r is modeled as

$$\nu_r = (C_s \tilde{\Delta})^2 \tilde{S}, \quad (4.20)$$

with $\tilde{S} = \sqrt{2\tilde{S}_{ij}\tilde{S}_{ij}}$ and the Smagorinsky constant $C_s = 0.17$.

If a passive scalar equation is solved along with the Navier-Stokes equations, the filtering process gives sub-grid fluxes j_i^r analogous to the sub-grid stresses. The sub-grid fluxes can for example be modeled by assuming gradient diffusion:

$$j_i^r = \frac{\nu_r}{Sc_t} \frac{\partial \tilde{\phi}}{\partial x_i} \quad (4.21)$$

Shortcomings of the Smagorinsky model are due to the constant C_s , which is not valid close to walls or in laminar regions. Furthermore, eddy-viscosity models with $\nu_r > 0$ do not allow for energy transfer from the small scales to the large scales (backscatter).

Dynamic models try to adjust C_s locally by applying two filter operations with different filter widths. The goal is then to find $C_s(x, t)$ that gives the best representation of the residual stresses on both filter levels. A modeling approach allowing for backscatter is the scale-similarity model, which is based on an extrapolation of the smallest resolved scales to the largest unresolved scales.

Another approach applying a somewhat different philosophy is the implicit modeling of the unresolved scales. The underlying idea is that the use of differencing schemes in finite volume methods is inevitably connected with truncation errors. The effect of the truncation error is in turn similar to the effect of the residual stresses, i.e. it is dissipative and tends to zero as the filter width is decreasing. Thus, instead of adding additional dissipation by introducing a model, the numerical dissipation can be used. Furthermore, it can be argued that the exact amount of dissipation is not important, as long as the resolution is good enough to resolve a large part of the inertial subrange, because this region is independent of viscosity (and so numerical viscosity) according to Kolmogorov's hypothesis.

Advantages with the implicit approach are its simplicity and straightforward formulation. Furthermore, it is superior to e.g. the Smagorinsky model in laminar regions or close to the walls, since Smagorinsky is too dissipative in these regions (C_S should be zero in these regions). In pulsating flow or in very complex geometries, where high anisotropy occurs, the modeling assumptions of turbulence models are not valid. Thus, implicit LES with high mesh resolution seems more adequate for these cases. Drawbacks with the implicit approach are higher grid-dependency, less control of the modeling and the lack of information about the unresolved turbulence properties. The latter is significant if wanting to model processes that occur at scales smaller than the resolved scales.

4.3. Boundary conditions

Another important aspect in flow computations as well as an important error source is the specification of the boundary conditions. This is the situation for engine computations where the correct boundary conditions to a great extent are difficult to specify due to pulsations and moving boundaries, e.g. valves and cylinders. Basically, the boundaries can be divided into walls and open boundaries, such as inlets and outlets.

The specification of the velocity on the walls is rather simple, since infinitely close to a wall the fluid has to have the same velocity as the wall, i.e. $u_i|_{wall} = 0$. More difficult is the boundary condition for the energy equation. One possibility is the assumption of adiabatic walls, equivalent to a zero-gradient condition on the temperature, i.e. $\frac{\partial T}{\partial x_i} n_i|_{wall} = 0$. However, if high temperature gradients between the fluid and the wall are present, there will be a significant heat transfer to (or from) the wall. This heat transfer is difficult to estimate. Another possibility is the specification of a constant wall temperature $T|_{wall} = const$. The true heat transfer may lie somewhere in between the adiabatic and the constant temperature conditions. For the simulation

of the concentration, a zero-gradient condition is applied on the walls, $\frac{\partial \phi}{\partial x_i} n_i|_{wall} = 0$, i.e. no mass transfer is allowed through the wall.

At flow inlets it is common to specify the mass flow rate since it can be estimated from engine data or one-dimensional computations. The pressure is set on the outlets. In the case of an inlet manifold, however, where the mass flow through the outlets is changing drastically in time due to the moving valves, it is beneficial to set the mass flow on the outlets and set the pressure on the inlet, where it is fairly constant. In the case of two species entering the flow domain at two inlets, one chooses usually to set $\phi = 1$ on one inlet and $\phi = 0$ on the other inlet, i.e. $\phi = 1$ means a concentration of 100% and $\phi = 0$ means 0%.

4.4. Numerics

The first task in all numerical simulations of a flow problem is the mesh creation. The mesh can be either structured or unstructured. A mesh is called structured if the distribution of nodes can be expressed as some function of the space coordinates. Otherwise the mesh is called unstructured since the node distribution is rather random, e.g. as a result of an automatic grid generator. Thereafter, the discretization scheme needs to be formulated, transforming the continuous equations onto the discrete mesh. In time-dependent problems a temporal discretization is needed as well. Furthermore, in order to numerically solve the discretized equations, a solution algorithm has to be defined. The approaches chosen during this thesis work are presented in this section.

4.4.1. Discretization

The discretization method used throughout this work is the finite-volume-method. Other methods available are discretization by finite differences and finite elements. Advantages of the finite volume method are the relatively simple implementation and broad applicability, e.g. for complex geometries. A short introduction will be given here for the example of the passive scalar equation (eq. 4.7). Integrating the equation over an arbitrary control volume V and applying Gauss' theorem delivers (Schäfer (1999))

$$\int_V \frac{\partial \phi}{\partial t} dV + \int_S (u_i \phi) n_i dS = \int_S (\kappa \frac{\partial \phi}{\partial x_i}) n_i dS, \quad (4.22)$$

where S is the surface of the control volume and n_i are the components of the surface normal vector. Three different terms can be identified; a temporal integral, an advective flux and a diffusive flux. The discretization of the temporal and spatial terms will be treated separately.

4.4.1a. *Spatial discretization.* For simplicity, the methods are illustrated by assuming a two-dimensional cartesian mesh with the notations shown in fig. 4.2. The control volume is split up into the plane sections defined by the grid points.² The purpose of

²In two dimensions, volumes obviously turn into surfaces and surfaces into curves, but in order to be consistent with the three-dimensional problem the original designations are kept

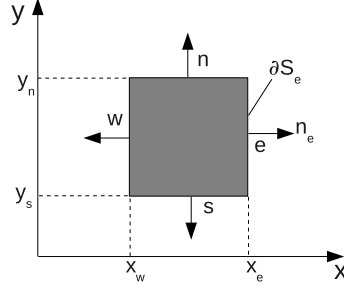


FIGURE 4.2. Control volume with designations - Sides s,w,n are designated in analogy to side e

the discretization is to approximate the integrals by values of ϕ on the grid points. In order to achieve this, the first step is the approximation of the integral by assuming a constant value of ϕ and $\frac{\partial\phi}{\partial x_i}$ over the surfaces of the control volume.

$$\int_S (u_i \phi) n_i dS \approx \sum_c u_i \phi_c n_{ci} \delta S_c \quad (4.23)$$

and

$$\int_S \left(\kappa \frac{\partial\phi}{\partial x_i} \right) n_i dS \approx \sum_c \kappa \left(\frac{\partial\phi}{\partial x_i} \right)_c n_{ci} \delta S_c \quad (4.24)$$

where the index c denotes the values on the middle of the surfaces.

The next task is to express ϕ_c and $\left(\frac{\partial\phi}{\partial x_i} \right)_c$ by the values of the neighboring grid nodes, which is the definition of the spatial differencing scheme. A simple scheme of second order for the advective term is the central differencing scheme. It is identical with a linear interpolation of the ϕ_c by the two neighboring nodes. For instance;

$$\phi_e \approx \phi_P + \frac{\phi_E - \phi_P}{x_E - x_P} \frac{x_e - x_P}{x_E - x_P} \quad (4.25)$$

In spite of its simplicity and formal accuracy of second order, the CDS (without modification) is useless in practical applications, since it allows for unphysical oscillations. It is therefore necessary to introduce damping in the form of artificial dissipation, flux-limiters or filters.

Another possibility is the use of upwind schemes. The simplest upwind scheme looks as follows;

$$\phi_e = \phi_P, \text{ for } \dot{m}_e > 0 \quad (4.26)$$

$$\phi_e = \phi_E, \text{ for } \dot{m}_e < 0 \quad (4.27)$$

When applying an upwind-scheme, information can only travel in the direction of the mass flow making oscillations impossible. Upwind schemes are especially useful in supersonic flows. However, for subsonic flows, upwind schemes tend to be dissipative since the interpolation error is of first order. It is also possible to build combinations of CDS and upwind schemes by using some mixing function.

The discretization of the diffusive fluxes is less problematic. The spatial derivative is most commonly approximated by central differences

$$\left(\frac{\partial\phi}{\partial x}\right)_e \approx \frac{\phi_E - \phi_P}{x_E - x_P}, \quad (4.28)$$

assuming linearity between the two neighboring points. This scheme gives an accuracy of second order and there are no limitations due to oscillations as for the advective schemes. Other schemes are possible, but practically seldom used.

4.4.1b. Temporal discretization. Similarly to the spatial discretization, the time domain is split up into finite time steps. A basic difference as compared to the spatial discretization is that the values of ϕ at a time t^n (where the superscript denotes the current time step) can only depend on values of ϕ at earlier time steps. Hence, the temporal discretization is always an extrapolation. For the presentation of the temporal discretization, eq. 4.22 is reformulated by denoting the discretization of the advective and diffusive fluxes by the operator $\mathcal{F}(\phi)$:

$$\int_V \frac{\partial\phi}{\partial t} dV = \mathcal{F}(\phi) \quad (4.29)$$

First, the time derivative can be assumed to be constant over the control volume

$$\int_V \frac{\partial\phi}{\partial t} dV \approx \frac{\partial\phi}{\partial t} \delta V, \quad (4.30)$$

leading to

$$\frac{\partial\phi}{\partial t} = \frac{1}{\delta V} [\mathcal{F}(\phi)]. \quad (4.31)$$

In principle one can distinguish between explicit and implicit schemes. An explicit scheme is of the following form,

$$\phi^{n+1} = \mathcal{F}(\phi^n, \phi^{n-1}, \dots), \quad (4.32)$$

where $\phi^n = \phi(t^n)$. Explicit schemes use only old values of ϕ , whereas implicit schemes use also the current time step;

$$\phi^{n+1} = \mathcal{F}(\phi^{n+1}, \phi^n, \phi^{n-1}, \dots). \quad (4.33)$$

Consequently, ϕ^{n+1} can not be determined directly by an implicit scheme, but has to be computed by an iterative algorithm.

Explicit schemes have the disadvantage, that the time step is limited by the fact that information must have 'enough time' to travel from one mesh node to the neighboring during one time step. This reasoning leads to the Courant-Friedrich limit (CFL)

on the time-step:

$$CFL = \frac{U \Delta t}{\Delta x} < 1 \quad (4.34)$$

For implicit schemes there is formally no such limit, however for LES applications a Courant number of about 1 is still recommended in order to resolve the smallest eddies also temporally.

A simple implicit scheme, the so called implicit Euler, scheme is defined by the backward difference,

$$\frac{\phi^{n+1} - \phi^n}{\Delta t} = \mathcal{F}(\phi^{n+1}), \quad (4.35)$$

applied for all computations in this work.

4.4.2. Solvers

The discretization of the Navier-Stokes equation leads to a linear equation system for each time step. This equation system can in principle be solved for all variables simultaneously (coupled solver). However, for low velocities, the equations become almost incompressible and stiff. The pressure equation is not well posed for these conditions, resulting in slow convergence and long computation times.

For subsonic problems, it is therefore more useful to solve the equations successively by so-called uncoupled or segregated solvers, originally developed for the incompressible equations. The basic principle of these solvers is to solve the momentum equations resulting from an estimated pressure field, e.g. the pressure of the previous time step. The solution of the momentum equations does in general not fulfill the mass conservation equation. Thus, the velocities, densities and the pressure have to be corrected in order to fulfill the mass conservation equations. This is done by solving a Poisson equation in order to update the pressure. With this pressure, the velocities and densities are updated. Repeating this procedure until convergence delivers a solution that fulfills both the momentum and mass conservation.

Several methods have been proposed for this implicit procedure. The most common ones are SIMPLE and PISO (for details see e.g. Ferziger & Peric (1996)). SIMPLE was originally developed for steady state problems and is very slow when applied to time-dependent calculations, PISO is faster but has some stability deficits, i.e. it is limited to small Courant numbers. In the computations throughout this thesis, a combination of SIMPLE and PISO named PIMPLE was used. For details see Weller (2005).

4.5. Evaluation of mixing quality

After a computation has been completed, the scalar concentration field is available. However, it is not obvious how to determine if the mixing is good or not. Perfect mixing would be achieved, if the concentration is the same everywhere in the region of interest for all times. Deviations from that perfect state occur in both space and time.

In stationary problems it is very common to use the uniformity index UI, calculated from the time-averaged concentration in a cross-section of the geometry. It is defined as:

$$UI = 1 - \frac{\int_A |c - \bar{c}_A| dA}{\int_A |c - \bar{c}_A| dA|_{ref}} \quad (4.36)$$

where c is the concentration in a cross-section, \bar{c}_A is the average of c in the cross-section. The denominator is a reference value, which should correspond to the maximum value of the integral. UI gives a simple measure between 0 and 1 for the uniformity of the mean concentration. Time information is, however, not included. One possibility is therefore to look at the RMS of the concentration in one point or a whole cross-section, which gives a measure of how much the concentration is fluctuating.

If one is interested on the effect of mixing on combustion, it might also be of interest to know how fast the fluctuations are, since long periods without EGR or oxygen will have more influence on the combustion than very short ones. One way to look at this, is the integral time scale of the scalar fluctuation, defined as:

$$\tau_c = \frac{1}{c'^2} \int_0^\infty (c'(t)c'(t+s)) d\tau \quad (4.37)$$

CHAPTER 5

Computations and Results

The overall aim with this study is to develop methods to compute the mixing processes occurring in EGR applications as accurate and realistic as possible. The approach is to assess the performance of different mixing models under engine-like conditions and to evaluate the sensitivity to the boundary conditions.

This section starts with the analysis of the flow in a T-junction with square cross-sections. This geometry is primarily used for the investigation of different scalar flux models within the RANS framework. The results are validated by experimental data. The second geometry studied is a T-junction with circular cross-sections. Also for this case, experimental data is available for validation purposes. Different turbulence and mixing models are applied for stationary and pulsating flow. Finally, the methods are applied to a realistic engine manifold provided by Scania.

5.1. Mixing process in a T-junction with square cross-section

5.1.1. Configuration

The configuration was chosen in order to resemble the geometry used in experiments by Hirota *et al.* (2006) (see figure 5.1). In this configuration, two air flows are mixed in a combining T-junction with a temperature difference of 48°C. The Reynolds number based on the inflow velocity and the hydraulic diameter of the main inflow is $2.5 \cdot 10^4$. A 2D-PIV system, using oil particles ($5\mu\text{m}$) as seeding particles, was used for the velocity measurements. Furthermore, the temperature was measured by a thermocouple rake. The inflow turbulence intensity was measured to about 5 %. However, it was found that the flow downstream of the junction is fairly independent of the inflow turbulence.

5.1.2. Meshes

In order to assess the grid sensitivity of the results, three meshes were used in this study. All meshes consist of structured, uniform hexahedral cells. The average cell size is 2mm for the coarse, 1mm for the intermediate and 0.5mm for the fine mesh. I.e., a cross-section of the main channel is resolved with 20x20 cells in the coarse mesh, 40x40 in the intermediate mesh and 80x80 cells in the refined mesh. The total amount of cells is 340,775, 1,816,316 and 5,452,800, respectively.

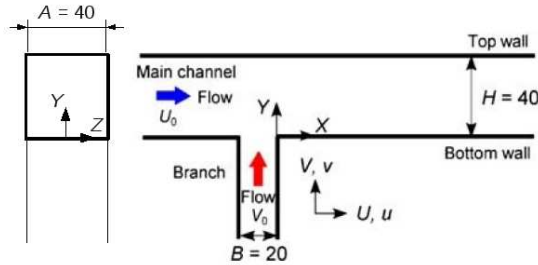


FIGURE 5.1. Sketch of the T-junction with square cross-sections, from Hirota *et al.* (2006)

5.1.3. Description of the flow (LES data)

The flow including the passive scalar was computed by implicit LES. The mean flow field in the center plane of the junction is shown in fig. 5.2. Directly downstream of the junction, a recirculation bubble is formed, i.e. negative velocities are present. The length of the recirculation bubble is approximately $1.9 \cdot H$, which is in good agreement with the experiment. Figure 5.3 displays velocity profiles at six different cross-sections. The size of the recirculation bubble is slightly increasing with finer mesh resolution. However, the overall agreement between the results is good. In figure 5.4, the RMS of the vertical velocity component v_{rms} is plotted for four of the above six cross-sections for the three meshes tested and the result is compared with experimental data. In the region of the recirculation bubble, the turbulence intensity exhibits two peaks; one due to high velocity fluctuations inside the bubble and the other due to turbulence production caused by the small velocity difference between the two flows. The first peak is under predicted by the computations, which might be explained by the fact that the particles used in the PIV method have too large inertia to follow the fast velocity fluctuations. The second peak is in good agreement with the experiments when compared to the finest mesh. The peak in the RMS due to the boundary layer, which has not been measured in the experiments, is rather mesh dependent. However, its influence on the region in the center of the pipe, where the actual mixing process is situated, is less significant.

Figure 5.5 shows the secondary flow vectors at the cross-sections $x/H=1$ and $x/H=7$ of the main channel. The background color shows the mean passive scalar. At $x/H=1$, there are two strong vortices present in the lower corners, similar to what was reported by Hirota *et al.* (2006). These vortices are formed due to the flow curvature of the flow coming from the branch and are similar to the so-called Dean vortices observed in bend pipes (see e.g. Hellström (2010)). However, the mixing process is not enhanced by these vortices since the vortices occur in a region where no scalar

gradient is present. Further downstream, at $x/H=7$, two large vortices are observed, transporting fluid upwards along the walls and downwards in the center of the pipe.

Thus, the main mixing mechanisms are the turbulent velocity fluctuations caused by the recirculation bubble and the strong velocity gradient above the recirculation. Further downstream, two large vortices are responsible for the mean mass transport in vertical direction.

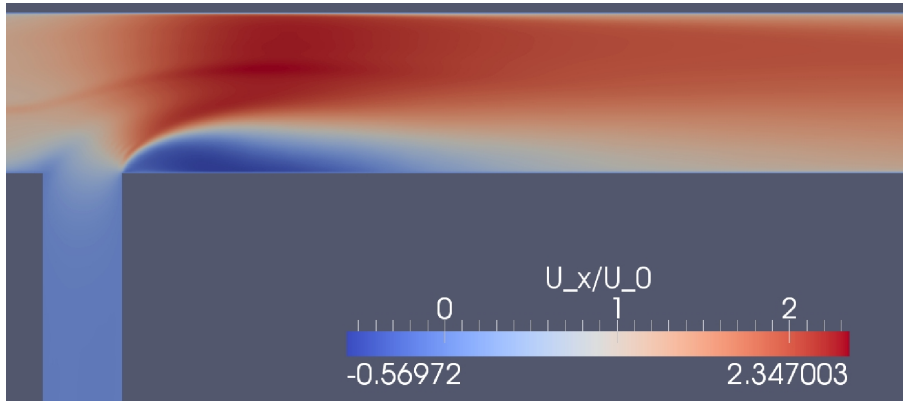


FIGURE 5.2. Mean streamwise velocity in the xy-plane

5.1.4. Evaluation of scalar flux models (RANS)

From the LES computation, the scalar fluxes $\overline{u'_i \phi'}$ can be calculated directly. As introduced in section 4.2.1, the scalar fluxes have to be modeled in a RANS computation. It is therefore possible to evaluate the passive scalar models (GDM and GGDM) by comparing the corresponding model expressions (equations 4.15 and 4.17) to the LES results. The computed flux vectors are shown in fig. 5.6. The Gradient diffusion model (GDM) provides a good agreement to the LES results in the beginning of the mixing layer. Further downstream a significant deviation from the gradient diffusion hypothesis, up to 45° , appears. As stated in Chapter 4, the gradient diffusion hypothesis is valid only for isotropic turbulence. Since the Generalized gradient diffusion model (GGDM) takes the Reynolds stresses into account, it is able to capture some of the anisotropic effects. A few diameters downstream of the junction, the flux vectors obtained by GGDM are diverging from the flow direction, which is in better agreement with LES. However, in the beginning of the mixing layer, where the greatest shear rates occur, the angle between the flux vector and the scalar gradient estimated by GGDM is far too great. Thus, none of the tested models is capable of predicting the correct flux direction.

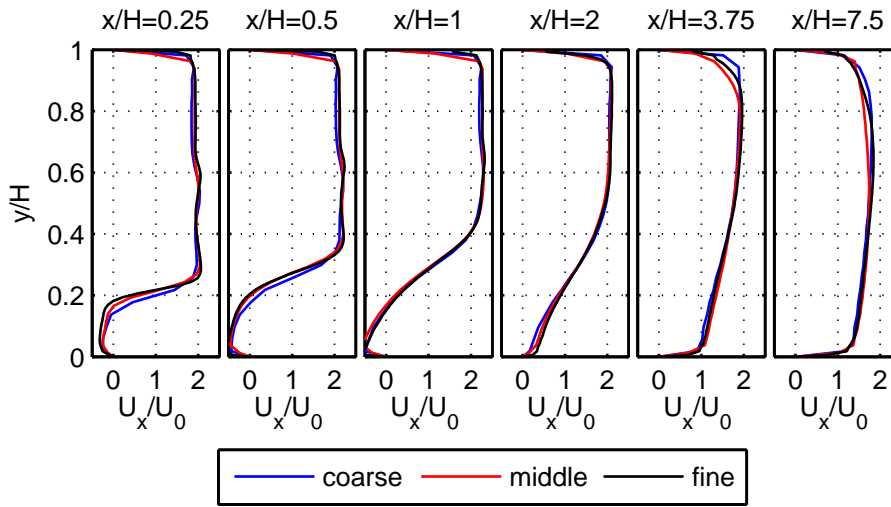


FIGURE 5.3. Mean streamwise velocity profiles in the xy -plane

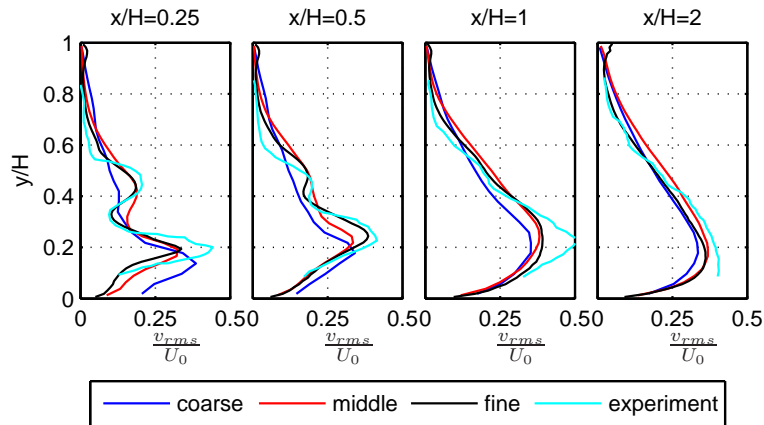


FIGURE 5.4. Turbulence intensity profiles in the xy -plane

5.2. Mixing process in a T-junction with circular cross-sections

5.2.1. Stationary boundary conditions

This section describes the flow and the mixing mechanisms in a T-junction with circular cross-sections (CC) (see fig. 5.7). For this geometry a mesh study has been performed (see paper 1). After studying the influence of the boundary conditions, an

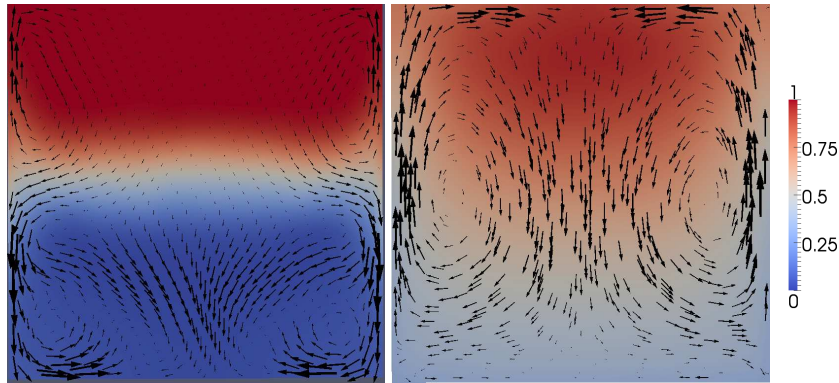


FIGURE 5.5. Mean velocity vectors and concentration at $x/H=1.0$ and $x/H=7.0$ from left to right

overview of the flow structures are presented and the turbulent instabilities are investigated based on the results obtained through implicit LES computations. Thereafter, a comparison to the k - ϵ -GDM model is presented. Experimental validation data for this case was provided by Vattenfall (see Westin *et al.* (2008)).

Inflow conditions

Flow computations are often sensitive to the specification of inflow conditions. This makes comparisons to experimental data difficult since the exact inflow conditions in experiments may not be documented well enough or are difficult to match in the set-up of the boundary condition in the computation. In RANS computations, it is possible to set the turbulence properties, e.g. k and ϵ , at the inlet boundaries. In LES (or DNS), an exact specification of the inflow turbulence requires a turbulent flow field on the inflow plane for each time step. This data is not trivial to obtain. It can be obtained from a separate computation with periodic boundary conditions or through the generation of turbulence properties by different deconvolution methods. A good overview is given in Keating *et al.* (2004).

In internal combustion engine applications, the complexity of the geometries makes it even more difficult to obtain the true inflow conditions since upstream curvature etc. are disturbing the inflow. Furthermore, it can be assumed that other factors such as pulsatility or swirl have a much greater influence on the results compared to the inflow turbulence.

For the T-junction with circular cross-section, a previous study showed that the flow past the junction was more or less independent of the inflow turbulence for stationary inflow [Westin *et al.* (2008)]. The junction of the two streams and the large velocity gradients are responsible for the turbulence production, making the inflow turbulence less important for this configuration.

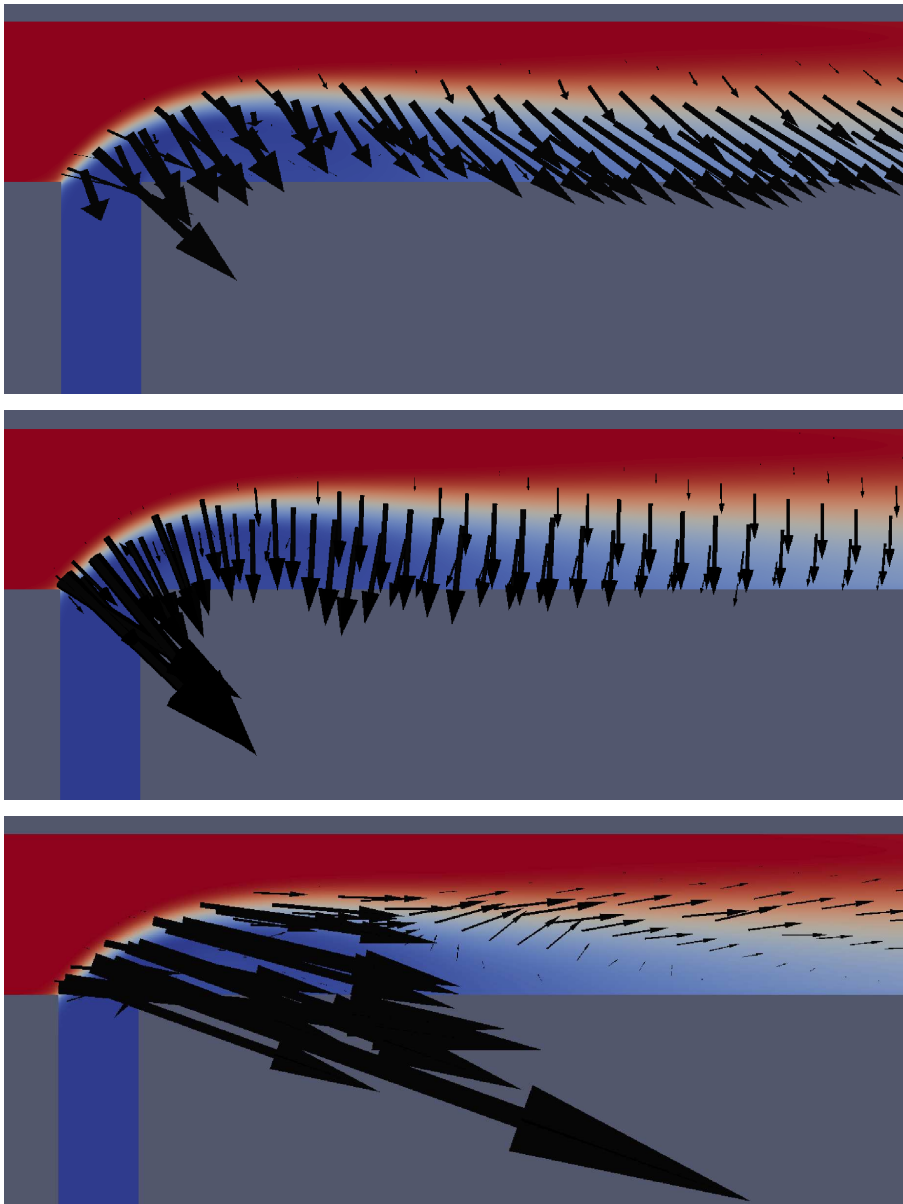


FIGURE 5.6. Flux vectors predicted by a) LES, b) GDM and c) GGDM (background: scalar distribution)

Thus, this section is limited to the influence of different constant velocity profiles. For the prescription of the velocity profile in a pipe, there are basically two possibilities. The first is to assume a top-hat profile, i.e. a constant velocity over the whole

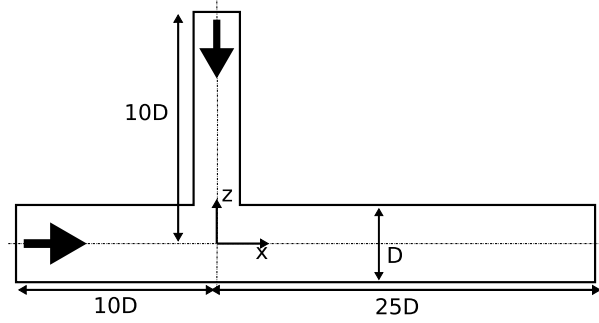


FIGURE 5.7. Computational domain of the T-junction with circular cross-sections

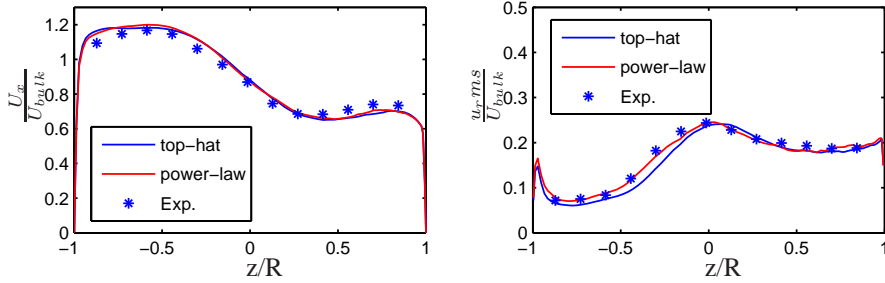


FIGURE 5.8. Axial velocity and RMS over z at $x/D=2.6$ for different inlet profiles

inlet plane. Another possibility is to receive a velocity profile from empirical turbulent pipe flow studies, e.g. a power-law profile as proposed by Prandtl (1952):

$$u/u_{max} = (1 - r/R)^{(1/n)} \quad (5.1)$$

where u_{max} is the maximum velocity in the middle of the pipe and n is dependent on the Reynolds number. $n=7$ seems, however, adequate for a wide range of Reynolds numbers. Eq. 5.1 is therefore referred to as Prandtl's-one-seventh-power-law.

Fig. 5.8 shows the velocity profiles and the velocity RMS at $x/D=2.6$ obtained by applying a top-hat and a power-law inlet velocity profile. No significant differences are visible. Thus, the results indicate that when the length of the inlet pipe is large enough (here $L_{inlet} = 10D$), it is not necessary to provide an exact specification of the inlet velocity profile.

Mean flow and secondary flow structures

The velocity field is similar to the square cross-section (SC) case. Fig. 5.9 shows the mean velocity and the turbulence intensity over some cross-sections downstream of

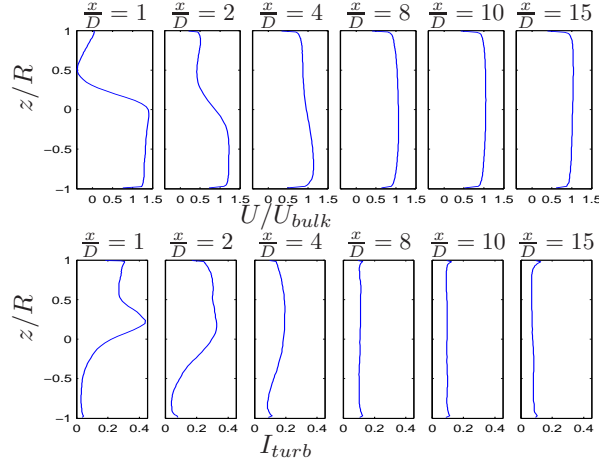


FIGURE 5.9. Mean velocity and turbulence intensity over some cross-sections

the junction. Downstream of the junction, there is a recirculation bubble with high levels of turbulence intensity. The high velocity gradient above the recirculation bubble is responsible for the turbulence production, resulting in a peak in the velocity RMS.

Fig. 5.10 shows some profiles of the mean passive scalar and the scalar RMS. The peak RMS is occurring at the position of the largest gradient of the passive scalar. This position does not coincide with the position of the greatest velocity gradient.

In the region of the recirculation, two longitudinal vortices are present that vanish rather quickly past the recirculation bubble (see fig. 5.11). The high turbulent fluctuations break up the vortices. As in the SC-case these vortices occur due to the curvature of the flow (Dean vortices). Further downstream, there are two larger vortices rotating in the opposite direction.

Spectral analysis

This section presents the spectral analysis performed for the T-junction with CC. This topic is treated more detailed in paper 1. Spectral analysis by using the Fourier transform of velocity and scalar signals are capable of detecting the inherent frequencies of turbulent instabilities or periodic phenomena in the flow field.

The strong shear layer described earlier, causes an instability in z -direction containing large turbulence production rates. Fig. 5.12 (left hand side) shows the power spectrum of the velocity component perpendicular to the shear layer (z -component). This figure displays the high amplitudes in the range between 300 and 450 Hz, attributed to the shear layer instability. Considering the y -component of the velocity in the same point (fig. 5.12 (right hand side)), another mechanism that takes places at a

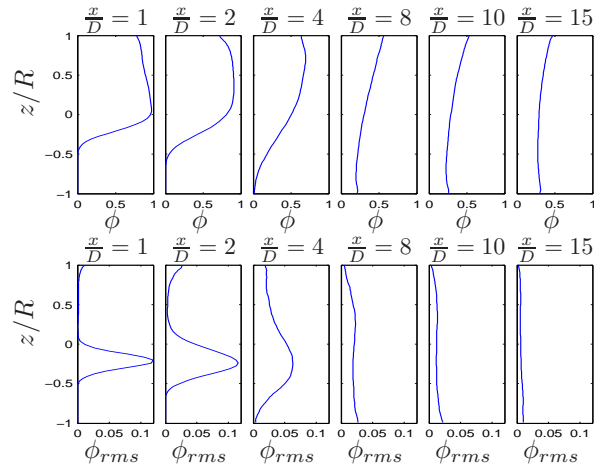


FIGURE 5.10. Profiles of the passive scalar and the RMS of the passive scalar

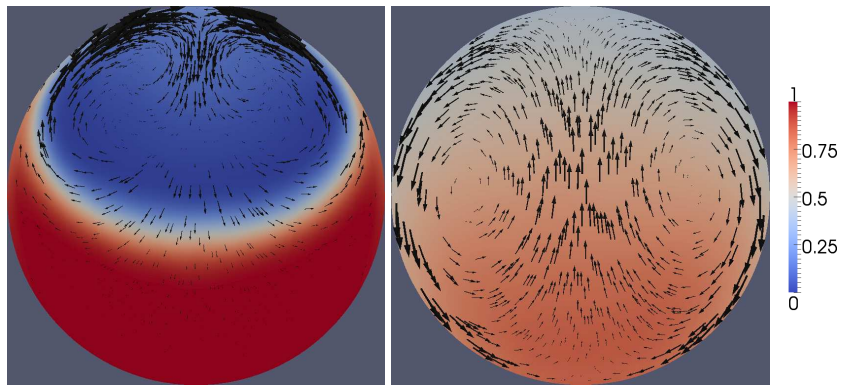


FIGURE 5.11. Mean velocity vectors and concentration at $x/D=1.0$ and $x/D=7.0$ from left to right, computed by LES

frequency of about 300 Hz is shown. This mechanism is a vortex shedding appearing behind the branch flow.

The corresponding scalar spectrum depicts a clear peak at 400 Hz, the shear layer instability frequency. Furthermore, a peak around 160 Hz is visible, due to the fact that low frequencies in the velocity spectrum are amplified in the scalar spectrum, whereas high frequencies are damped out.

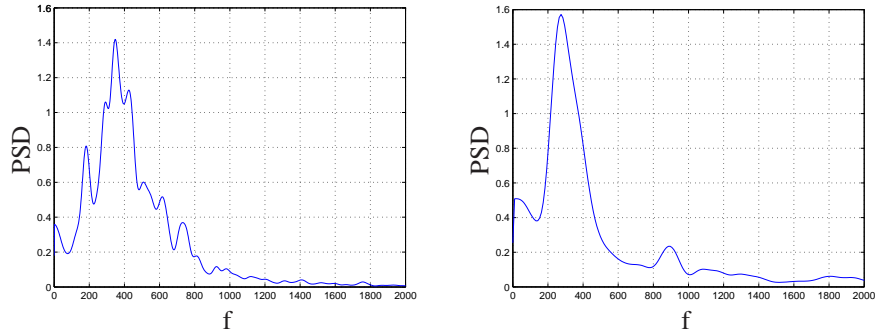


FIGURE 5.12. Power spectral density of U_z (left) and U_y (right) inside the shear layer at $x/D = 1.5$, $y/D = 0$, $z/D = 0.15$ (stationary case)

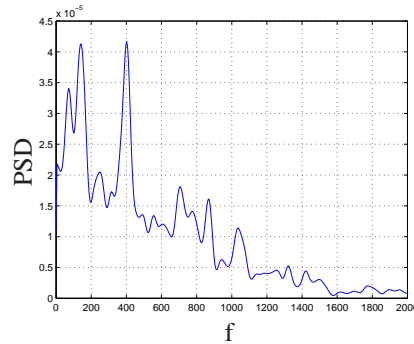


FIGURE 5.13. Power spectral density of ϕ inside the shear layer at $x/D = 1.5$, $y/D = 0$, $z/D = 0.15$ (stationary case)

Comparison to RANS

The different turbulence and mixing models introduced in chapter 4 are compared in this section. The implicit LES modeling is compared to the widely used $k-\epsilon$ -RANS model in combination with the GDM.

Fig. 5.14 shows the in-plane velocities and the scalar distribution at the cross-sections $x/D=1$ and $x/D=7$ (comp. fig. 5.11) computed by $k-\epsilon$. Apparent also in the $k-\epsilon$ -computation, are the vortices due to the curvature of the flow at $x/D=1$. However, in contrast to the LES simulations, these vortices maintain their strength in axial direction. The vortices are still observed at $x/D > 10$. In the LES simulation, the large turbulence intensities inside the recirculation zone break up the vortices and enable the possibility for the development of vortices rotating in the opposite direction. This feature cannot be captured by RANS, since the velocity fluctuations are smoothed out.

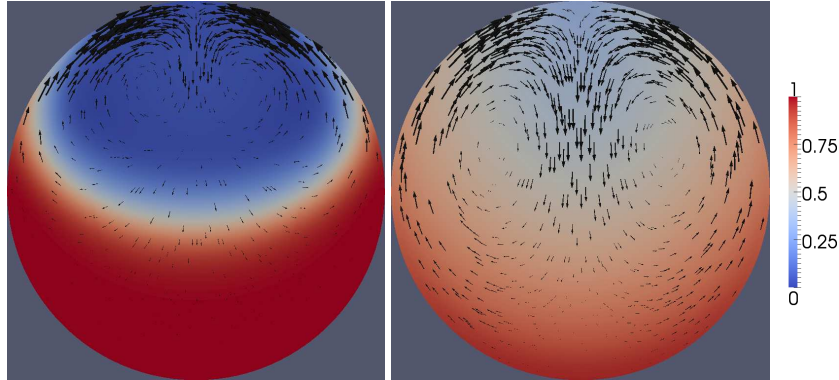


FIGURE 5.14. Mean velocity vectors and concentration at $x/D=1.0$ and $x/D=7.0$ computed by RANS-k- ϵ , note the difference to fig. 5.11

As a consequence, the scalar field in the RANS computation is largely differentiating to that observed in the LES computation. Overall, the RANS computation is too diffusive and provides too little mixing. This could of course be adjusted by changing the model parameters. However, this approach would lack generality, i.e. general conclusions cannot be drawn that could be applied to other geometries and boundary conditions.

5.2.2. Pulsating boundary conditions

The influence of incoming pulsations on the mixing process is studied by the specification of a time-varying mass flow on the branch inlet. The inlet mass flow is sine-shaped and has an amplitude of 100% of the mean mass flow, i.e. the mass flow on the branch inlet is given by $\dot{m}(t) = \dot{m}_{stat}(1 + \frac{1}{2}\sin(2\pi \cdot f \cdot t))$. Three cases with different pulsation frequencies ($f = 30Hz, f = 60Hz$ and $f = 300Hz$) were simulated and are compared in this section. The Strouhal numbers for these frequencies, defined as

$$St = \frac{fD}{U}, \quad (5.2)$$

are 0.05, 0.1 and 0.5, respectively.

Spectral analysis

In order to point out some important phenomena in pulsating flow, the spectral analysis in section 5.2.1 is now extended to the pulsating cases, i.e. the power spectra showing the instabilities in stationary flow are compared to the pulsating cases. Fig. 5.15 shows such a comparison for the velocity fluctuations inside the recirculation bubble.

For low pulsation frequencies ($f = 30 Hz$ and $f = 60 Hz$) the behavior resembles to the stationary flow situation. The natural instabilities are still visible at frequencies

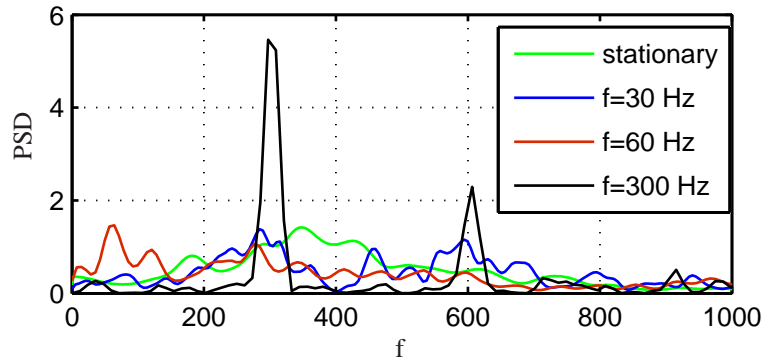


FIGURE 5.15. Power spectral density of velocity signal U_z inside the shear layer for different inflow pulsation frequencies and for stationary inflow. A resonance effect between the natural frequencies and the pulsation frequency can be observed.

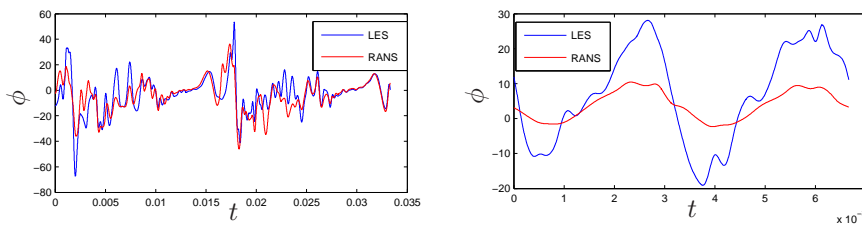


FIGURE 5.16. U_z inside the shear layer for 2 pulsation periods computed by RANS and LES, for $f=60\text{Hz}$ (left) and $f=300\text{Hz}$ (right)

around 350 Hz. If the pulsation frequency reaches the range of the natural instabilities, resonance effects can be observed. The natural instabilities are amplified by the inflow pulsations and dominate the spectrum. This implies that the flow cannot be described as quasi-stationary.

In RANS, the scales at which these phenomena occur are modeled. The interaction between pulsation frequencies and turbulent instabilities can therefore not be predicted by RANS methods. This is illustrated in fig. 5.16, showing a comparison of the velocity inside the shear layer, predicted by RANS and LES.

5.3. Comparison of the mixing quality for the two junctions (stationary flow)

The mixing measures introduced in section 4.5 are now compared for the two junctions with square and circular cross-sections. Only stationary flow is considered here. Fig. 5.17 compares the uniformity index (UI), the RMS of the concentration and the

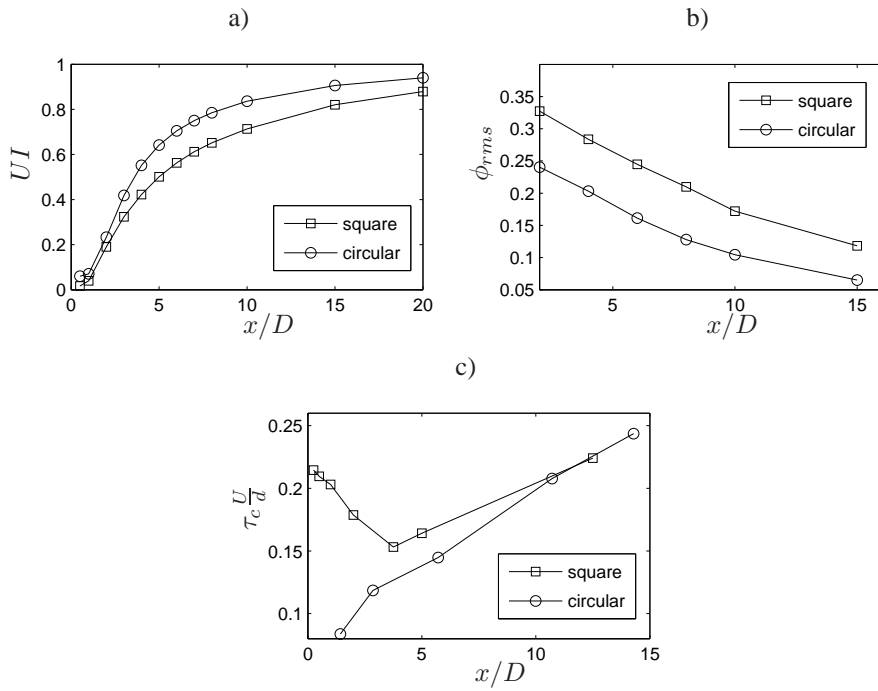


FIGURE 5.17. Different mixing quality indicators, a) Uniformity index, b) ϕ_{rms} on the center line, c) $\tau_c \frac{U}{d}$ on the center line

normalized time scale of the concentration fluctuations. Both the UI and the RMS indicate, that the mixing quality is better in the circular cross-section case. The time scale is much smaller for the circular cross-section case directly behind the junction, but is converging to the same order as the square cross-section case further downstream. The reason for the discrepancy might be found in the higher complexity of the geometry; producing faster, more irregular velocity and scalar fluctuations.

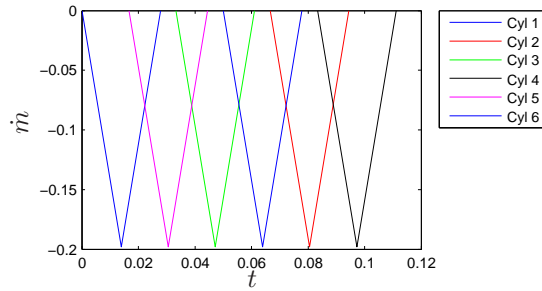


FIGURE 5.18. Time dependent mass flow specified on the outlet boundaries

5.4. Scania Manifold

The computations on the 6-cylinder Diesel engine manifold provided by Scania are performed with generic boundary conditions showing the effect of inlet pulsations and different modeling approaches. Since the results are discussed in detail in Paper 2, this section will give a short summary.

Computations were performed using LES and unsteady RANS with constant and pulsating sinus-shaped EGR inflow. On the outlet, a time dependent mass flow mimicking the valve motions was approximated as triangular functions (see fig. 5.18). The computations show, that the EGR concentration is highly unsteady and can vary up to 10% in time. Averaged over several engine cycles, the cylinder-to-cylinder deviation is only about $\pm 2\%$. However, if one is interested in the effects of the EGR distribution on the combustion, the instantaneous concentration is of importance.

The variation of the inlet conditions showed that EGR pulses are travelling down the manifold without being destroyed by turbulence, emphasizing that the correct prescription of the inlet conditions is crucial for the computation results in the presence of pulsations (see fig. 5.19).

Discussing the differences between RANS and LES, it can be stated that RANS is too diffusive. Large local concentration differences can be seen in regions, where the LES results indicate a rather uniform distribution. For the case of pulsating inflow conditions, the difference between the modeling approaches is small due to the fact that the turbulent mixing rate is much smaller than the pulsations. This could, however, change at low pulsation frequencies or when running into resonances with natural instabilities as has been shown in the preceding chapter.

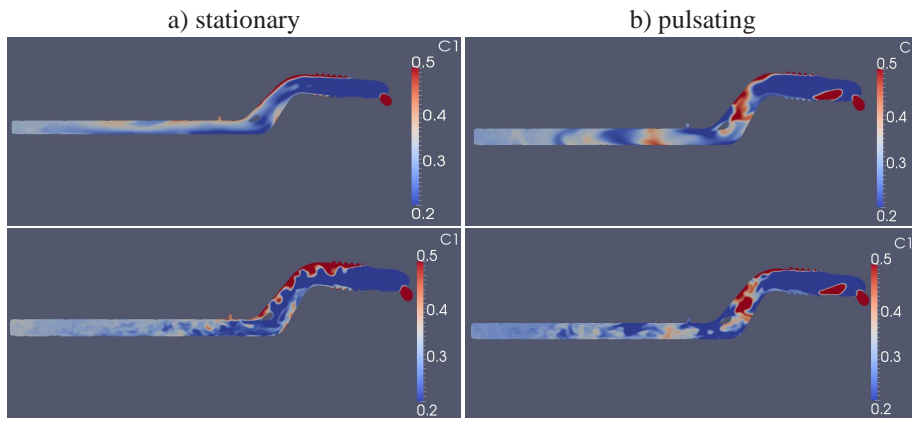


FIGURE 5.19. Instantaneous concentration at the same instant of time computed by RANS (top) and LES (bottom) for a) stationary and b) pulsating EGR flow

CHAPTER 6

Conclusions and outlook

Mixing flows have been computed in different generic geometries and in an engine manifold. LES and RANS were compared and the flow structures were analyzed. The main conclusions are:

- The assumptions behind the RANS models for passive scalar fluxes (GDM and GGDM) are not valid, even in a fairly simple geometry as a T-junction with square cross-sections.
- The computations on the T-junction with circular cross-sections showed that RANS predicts completely different secondary flow structures and mixture distributions from LES results. The reason for that is that the break-up of secondary structures by turbulence cannot be captured by RANS.
- Natural instabilities of the shear layer were examined by LES. Resonance effects with inflow pulsations could be observed. These effects cannot be seen in RANS calculations, since RANS models filter out these scales of turbulent motion.
- The studies on the engine manifold show that the effect of pulsating boundary conditions is important. The smoothing effect of URANS does not seem to be adequate for accurate mixing computations, when turbulence is governing the mixing. If strong pulsations are present LES and RANS are in better agreement due to turbulence being less important.

The work described in this thesis shows that LES provides a promising framework for the computation of mixing processes occurring in EGR applications. The RANS approach is questionable due to the complexity of the geometry and pulsating flow effects.

Future work will therefore focus on aspects of LES computations. More realistic boundary conditions will be applied, taken from one-dimensional engine simulations. The effect of small changes in the boundary conditions will be evaluated. Furthermore, other geometries will be considered and the computations will be compared to experiments, when possible, in order to gain more generality and insight into the important mixing mechanisms.

Acknowledgements

First of all, I would like to thank my supervisor Laszlo Fuchs for guidance and waking me up on monday mornings. My second supervisor Lisa PrahL Wittberg is acknowledged for her comments on this thesis.

Furthermore, the financial support by the CCGEx competence center and the swedish vehicle industry is greatly acknowledged. Special thanks go to Scania for providing geometries, meshes and feedback. Also Vattenfall is acknowledged for providing experimental data.

The most important help throughout this thesis was, however, given by all my colleagues at the mechanics department and at the internal combustion department. Thanks for fruitfull discussions, nice fika breaks and afterworks!

At last, I would like to thank my girlfriend Hanna for appreciating the beauty of my vortices.

References

- BATCHELOR, G. 1959 Small-scale variation of convected quantities like temperature in turbulent fluid, part 1. *Journal of Fluid Mechanics* **5**, 113–133.
- BATCHELOR, G., HOWELLS, I. & TOWNSEND, A. 1959 Small-scale variation of convected quantities like temperature in turbulent fluid, part 2. *Journal of Fluid Mechanics* **5**, 134–139.
- CHAUVET, T. & DIMITROVA, Z. 2008 Synergies between high egr operation and gdi systems. *SAE Technical Paper 2008-01-0134*.
- DIETSCH, K.-H. & KLINGEBIEL, M. 2007 *Automotive Handbook*, 7th edn. Bosch.
- FERZIGER, J. H. & PERIC, M. 1996 *Computational Methods for Fluid Dynamics*. Springer.
- HELLSTRÖM, F. 2010 Numerical computations of the unsteady flow in turbochargers. PhD thesis, KTH Stockholm.
- HEYWOOD, J. B. 1988 *Internal Combustion Engine Fundamentals*. McGraw-Hill, New York.
- HIROTA, M., ASANO, H., NAKAYAMA, H., ASANO, T. & HIRAYAMA, S. 2006 Three-dimensional structure of turbulent flow in mixing t-junction. *JSME International Journal Series B* **49**, 1070–1077.
- HU, L. & KAZIMI, M. 2006 Les benchmark study of high cycle temperature fluctuations caused by thermal striping in a mixing tee. *International Journal of Heat and Fluid Flow* **27**, 54–64.
- KARTHIKEYAN, S., HARIGANESH, R., SATHYANADAN, M. & KRISHNAN, S. 2011 Computational analysis of egr mixing inside the intake system & experimental investigation on diesel engine for lcv. *International Journal of Engineering Science and Technology* pp. 2050–2058.
- KEATING, A., PIOMELLI, U. & BALARAS, E. 2004 A priori and a posteriori tests of inflow conditions for large-eddy simulation. *Physics of fluids* **16** (12), 4696–4712.
- KOLMOGOROV, A. N. 1991 The local structure of turbulence in incompressible viscous flow for very large reynolds numbers. *Proc. R. Soc. London A* **434**, 9–13.
- KUCZAJ, A., KOMEN, E. & LOGINOV, M. 2010 Large-eddy simulation study of turbulent mixing in a t-junction. *Nuc. Eng. Des.* doi:10.1016/j.nucengdes.2009.11.027.
- MAIBOOM, A., TAUZIA, X. & HETET, J.-F. 2009 Influence of egr unequal distribution from cylinder to cylinder on nox-pm trade off of a hsdie automotive diesel engine. *Applied Thermal Engineering* **29**, 2043–2050.
- POPE, S. 2008 *Turbulent Flows*. Cambridge University Press.

- PRANDTL, L. 1952 *Essentials of Fluid Dynamics*. Blackie, London.
- REIFARTH, S. 2010 *EGR-Systems for Diesel Engines*. KTH Stockholm.
- SCHÄFER, M. 1999 *Numerik im Maschinenbau*. Springer, Berlin.
- SCHWARZ, H., DECKER, H., ROHDE, S., FELGER, G., LEMBKE, M., ZEHNALL, M., GUENTHER, D., KRAUS, B. & DIETER, W. 1988 Avgasteknik för ottomotorer - teknisk information. Bosch.
- STANGLMAIER, R. H. & ROBERTS, C. E. 1999 Homogenous charge compression ignition (hcci): Benefits, compromises, and future engine application. *SAE Technical Paper 1999-01-3682* .
- WALKER, C., MANERA, A., NICENO, B., SIMIANO, M. & PRASSER, H.-M. 2010 Steady-state rans-simulations of the mixing in a t-junction. *Nuc. Eng. Des.* **doi:10.1016/j.nucengdes.2010.05.056**.
- WELLER, H. 2005 Pressure-velocity solution algorithms for transient flows. *Technical Report TR/HGW/05, OpenCFD Ltd.* .
- WESTIN, J., T'MANNETJE, C., ALAVYOON, F., VEBER, P., ANDERSSON, L., ANDERSSON, U., ERIKSSON, J., HENRIKSSON, M. & ANDERSSON, C. 2008 High-cycle thermal fatigue in mixing tees. large-eddy simulations compared to a new validation experiment. *ICONE Proceedings* .
- YOSHIZAWA, K., MORI, K., MATAYOSHI, Y. & KIMURA, S. 2003 Development of an exhaust gas recirculation distribution prediction method using three-dimensional flow analysis and its application. *Journal of Engineering for Gas Turbines and Power* **125**, 1066–1074.

